

FRONTIERS OF REMOTE SENSING INFORMATION PROCESSING

Editor: C H Chen

*University of Massachusetts-Dartmouth &
Information Research Laboratory, Inc. USA*

2003



World Scientific
New Jersey • London • Singapore • Hong Kong

Published by

World Scientific Publishing Co. Pte. Ltd.
5 Toh Tuck Link, Singapore 596224
USA office: Suite 202, 1060 Main Street, River Edge, NJ 07661
UK office: 57 Shelton Street, Covent Garden, London WC2H 9HE

British Library Cataloguing-in-Publication Data

A catalogue record for this book is available from the British Library.

FRONTIERS OF REMOTE SENSING INFORMATION PROCESSING

Copyright © 2003 by World Scientific Publishing Co. Pte. Ltd.

All rights reserved. This book, or parts thereof, may not be reproduced in any form or by any means, electronic or mechanical, including photocopying, recording or any information storage and retrieval system now known or to be invented, without written permission from the Publisher.

For photocopying of material in this volume, please pay a copying fee through the Copyright Clearance Center, Inc., 222 Rosewood Drive, Danvers, MA 01923, USA. In this case permission to photocopy is not required from the publisher.

ISBN 981-238-344-1

Printed by Fulsland Offset Printing (S) Pte Ltd, Singapore

CHAPTER 11

RECONSTRUCTION AND RESOLUTION ENHANCEMENT TECHNIQUES FOR MICROWAVE SENSORS

David G. Long

*Electrical and Computer Engineering Department
459 Clyde Building, Provo, UT 84602
E-mail: longee.byu.edu*

Microwave remote sensing instruments such as radiometers and scatterometers have proven themselves effective in a variety of Earth Science studies. The resolution of these sensors, while adequate for many applications, is a limiting factor to their application in other studies. As a result, there is a strong interest in developing ground processing methods which can enhance the spatial resolution of the data. A number of resolution enhancement algorithms have been developed based on inverse filtering and irregular sampling reconstruction. This Chapter discusses the use of resolution enhancement and reconstruction algorithms in microwave remote sensing. While the focus is on microwave instruments, the techniques and algorithms considered are applicable to a variety of sensors, including those not originally designed for imaging.

1. Introduction

There are many types of remote sensing instruments, including optical, infrared, and microwave sensors. Microwave remote sensing instruments can be divided into two broad classes: passive (radiometers) and active (radars)⁵⁵. Active microwave sensors can be further divided into four general classes: synthetic aperture radar (SAR) systems, scatterometers, altimeters, and weather radars. SAR systems are generally high resolution (100 m and finer) while spaceborne radiometers and scatterometers tend to be low resolution sensors (12 km to 75 km). The resolution of these latter sensors is suitable for the oceanic and atmospheric applications for which they were designed, but there is growing interest in applying such microwave sensor data to new applications requiring better resolution.

Further, while the next generation of spaceborne microwave sensors may have somewhat higher resolution, the extensive datasets of radiometer and scatterometer data offer an important baseline for studies of global change. This has resulted in interest in enhancing the resolution of historic microwave sensor data to facilitate comparison with higher resolution sensor data. To meet this need a number of algorithms for spatial resolution enhancement have been successfully developed and enhanced resolution microwave data is now being used operationally.

This Chapter considers the theory and methods of spatial resolution enhancement of microwave remote sensing data. While the focus is on spaceborne radiometers and scatterometers, the general reconstruction and enhancement theory discussed can be applied to a variety of sensors and applications, including creating images from sensors not originally designed for imaging. Section 2 provides background on the sensors considered. Section 3 provides background in resolution enhancement, contrasting inverse filtering, extrapolation, and reconstruction methods. The theory of irregular reconstruction is developed and algorithms for enhanced resolution reconstruction are considered. Section 4 considers the application of the technique to data from Earth Resources Satellite (ERS) -1 and -2 Active Microwave Instrument (AMI) scatterometer mode (hereafter termed ESCAT). Simulations are used to evaluate the effectiveness of the algorithms, along with actual data. A conclusion is provided in Section 5.

2. Spaceborne Microwave Sensors

A variety of active and passive microwave remote sensing instruments have flown in space. Some of these have collected long time series such as the Special Sensor Microwave Imager (SSM/I) radiometer¹⁸, flown on Defense Meteorological Satellite Program (DMSP) spacecraft since the early 1980's, ESCAT² operating from 1982, and the SeaWinds instrument⁵⁰ operating aboard QuikSCAT since 1999. Prior sensors include the NASA Scatterometer (NSCAT)³⁸ which operated in 1996 and 1997, the Seasat Scatterometer (SASS)²³ and Multichannel Microwave Radiometer³⁹ both in 1978, and the Nimbus radiometer series operating in the late 1970's, among others. Together these instruments have demonstrated the utility of microwave sensors in the study and monitoring of the Earth's land, ocean, and atmosphere. The global coverage, but low resolution, of these sensors complements the high resolution, but limited coverage, of SAR systems.

Radiometers are passive, receive-only sensors which measure the thermal emission (brightness temperature) of the target in the microwave band⁵⁵. The apparent scene brightness temperature is related to the emissivity and temperature of the surface and is modified by the intervening atmosphere. By appropriate selection of operating frequencies in several microwave bands, the temperature and moisture content of the atmosphere²², as well as key surface properties such as land surface temperature³⁷, soil and plant moisture^{20,42}, sea-ice mapping⁵⁴, snow cover classification¹⁶, and wind speed (over the ocean)⁵⁷, can be retrieved. Radiometer data is being operationally used in weather forecasting and sea-ice monitoring.

Scatterometers are real aperture radars that operate by transmitting a pulse of microwave energy towards the Earth's surface and measuring the reflected energy. The backscattered energy is related to the normalized radar cross-section (σ°) via the radar equation⁵⁵. The spatial response function of the sensor determines the spatial resolution of the σ° observation, with typical resolutions varying from 25 to 50 km. Originally designed for retrieval of near-surface winds over the ocean,

scatterometer data is also being applied to the study of tropical vegetation, polar ice, and global change^{26,29,33,34,59}. Like radiometer data, scatterometer data is operationally used in weather forecasting and sea-ice monitoring.

2.1. Radiometers

A radiometer measurement is the integral of the product of the scene brightness and the antenna pattern. The i^{th} measurement $T_a(i)$ (in K) is obtained by integrating the product of surface brightness response $T_b(x, y)$ and the antenna gain pattern at the surface $G_i(x, y)$,^{13,55}

$$T_a(i) = \overline{G}_i^{-1} \iint G_i(x, y) T_b(x, y) dx dy, \quad (1)$$

where

$$\overline{G}_i = \iint G_i(x, y) dx dy. \quad (2)$$

The integrals are over the surface area corresponding to the non-negligible gain of the antenna. The dependence of G on i arises from the boresight pointing of the antenna which changes as the antenna scans the surface. Note that the antenna pattern acts as a low pass filter of the surface brightness, limiting the effective spatial resolution of the measurement to approximately the 3 dB beamwidth. Radiometer measurements are “noisy” due to the limited integration time available for each measurement.

2.2. Scatterometers

A radar scatterometer is designed to determine the normalized radar cross section (σ°) of the surface. The primary application of spaceborne scatterometers have been the measurement of near-surface winds over the ocean. By combining σ° measurements from different azimuth angles, the near-surface wind vector over the ocean's surface can be determined using a geophysical model function^{23,38} which relates wind and σ° . The scatterometer directly measures σ° via measuring the backscattered power from a transmitted pulse. Due to thermal noise in the receiver, radiometric noise and speckle, the power measurement is corrupted by noise. A separate measurement of the noise-only power is subtracted from the signal+noise measurement to yield the backscattered power “signal” measurement P_S . The observed σ° is then computed using the radar equation⁵⁵. Ignoring the incidence angle dependence of σ° , the radar equation can be approximately expressed as

$$P_S = \iint \frac{P_T G(x, y) \lambda \sigma^\circ(x, y)}{(4\pi)^3 R^4(x, y)} dA = \iint h(x, y) \sigma^\circ(x, y) dA \quad (3)$$

where P_T is the transmit power, $G(x, y)$ is the antenna gain pattern on the surface, dA is the differential area, $R(x, y)$ is the slant range, $\sigma^\circ(x, y)$ is the surface σ° , $h(x, y)$ is the equivalent spatial response function, and the integrals are over the

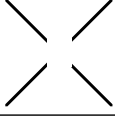

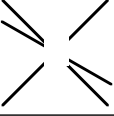
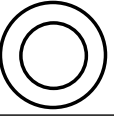
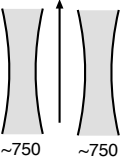

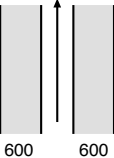

	SASS	ESCAT	NSCAT	SeaWinds
FREQUENCY	14.6 GHz	5.3 GHz	13.995 GHz	13.6 GHz
ANTENNA AZIMUTHS				
POLARIZATIONS	V-H, V-H	V ONLY	V, V-H, V	V-OUTER/H-INNER
BEAM RESOLUTION	FIXED DOPPLER	RANGE GATE	VARIABLE DOPPLER	PENCIL-BEAM
SCIENCE MODES	MANY	SAR, WIND	WIND ONLY	WIND/HI-RES
RESOLUTION (σ°)	50 km	50 km	25 km	Egg: 25x35 km Slice: 6x25km
SWATH, km	 ~750 ~750	 500	 600 600	 1400, 1800
INCIDENCE ANGLES	0° - 70°	18° - 59°	17° - 60°	45° & 54.4°
DAILY COVERAGE	VARIABLE	< 41 %	78 %	92 %
MISSION DATES	SEASAT: 6/78 - 10/78	ERS-1: 92-96 ERS-2: 95-01(?)	ADEOSI: 8/96 - 6/97	QuikSCAT: 6/99 - ADEOSII: 12/02

Fig. 1. Scatterometer Comparison

surface area corresponding to the non-negligible gain of the antenna and/or signal processing filters. Given P_S , the observed σ° is computed as $\sigma^\circ = X^{-1}P_S$ where

$$X = \iint \frac{P_T G(x, y) \lambda}{(4\pi)^3 R^4(x, y)} dA = \iint h(x, y) dA. \quad (4)$$

A summary comparison of the wind scatterometers that have flown in space is shown in Fig. 1. SASS, NSCAT and ESCAT used a fan-beam antenna configuration while SeaWinds employs a dual rotating pencil-beam antenna. In a fan-beam scatterometer, along-track resolution is obtained by a combination of a narrow antenna pattern and the timing of transmit pulses integrated into a single measurement cell. Cross-track resolution is obtained either by range gate filtering (ESCAT) or by Doppler filtering (SASS and NSCAT)³⁸. ESCAT is described in greater detail later.

While a scanning scatterometer collects measurements at a constant incidence angle⁵⁰, fan-beam scatterometers measure σ° at a variety of incidence angles. Since the target response varies with incidence angles, a model for the incidence angle dependence of the target response is used to generate normalized images. Over most natural surfaces within the incidence angle range $20^\circ \leq \theta \leq 60^\circ$, corresponding to the range of scatterometer measurements, a linear model for σ° (in dB) as a function

of incidence angle can be used^a, i.e. $\sigma_{\text{dB}}^{\circ}(\theta) = \mathcal{A} + \mathcal{B}(\theta - 40^{\circ})$ where \mathcal{A} is the 40° incidence angle-normalized σ° and \mathcal{B} is the dependence of σ° on the incidence angle θ . The \mathcal{A} and \mathcal{B} coefficients are functions of the geophysical properties of the surface. Note that 40° is the approximate center incidence angle over the swath and is a convenient angle for making comparative analyses.

As previously noted, scatterometer measurements are noisy. The measurement accuracy is frequently expressed in terms of the normalized standard deviation, or K_p of the measurements³⁶. K_p is sometimes known as the “scatterometer radiometric accuracy”. For ERS-1 $K_p(k)$ is approximately 5%. For SASS, NSCAT, and SeaWinds $K_p(k)$ varies from as low as 1% to 15%, though it is sometimes higher.

Reconstruction and resolution enhancement methods can be applied to other real aperture radars as well. For example, the Tropical Rain Mapping Mission (TRMM) Precipitation Radar²⁴, while it employs range resolution to map the vertical profile of rain, it also makes real-aperture surface backscattering measurements which can be applied in scientific studies^{8,30,51}.

3. Reconstruction and Resolution Enhancement

The resolution of scatterometers and radiometers is adequate for ocean applications but is too coarse for many land and ice applications. However, because of frequent global coverage, they are desirable candidates for resolution enhancement algorithms. Since the data from these instruments is used in geophysical studies, accuracy is crucial in resolution enhancement. Further, an improvement in the actual *effective* resolution of the data is expected from such algorithms. While it is tempting to interpolate the available data onto a high resolution grid in an attempt to make the pixel size (sometimes called the *pixel resolution*) finer, this does not improve the *effective* resolution of the resulting image. While various definitions of effective resolution exist^{21,25}, a common working definition is the resolving capability for two closely spaced objects. The objects are considered individually “resolved” if there is a 3 dB change in image value between them against a high contrast background. The gap between the objects defines the effective resolution.

Algorithms for spatial resolution enhancement can be divided into three broad categories: extrapolation, ad hoc techniques, and reconstruction. Extrapolation algorithms can be further divided into two classes: pure extrapolation and multi-channel extrapolation. The former includes algorithms which use maximum entropy to extrapolate techniques the signal spectrum. Based on our common experience in polynomial extrapolation, extrapolation must be used with caution since it can

^aWhile not applicable for all targets, over the Amazon Rainforest (which exhibits high volume scattering) a “gamma” normalization may be used with some success, i.e.,

$$\gamma(k) = \sigma^{\circ}(k) / \cos \theta(k)$$

where $\theta(k)$ is the incidence angle of the k^{th} measurement of σ° . Over the incidence angle range $[20^{\circ}, 60^{\circ}]$, $\gamma(k)$ is approximately constant.

produce misleading results.

Multi-channel extrapolation algorithms have been used with success with microwave data^{3,48}. These algorithms rely on the collection of observations at several different frequency channels which have differing spatial resolutions. The goal of the algorithm is to extrapolate the signal characteristics of the coarse resolution channels to be commensurate with the resolution of the fine resolution channels based on the correlation in the target response between the channels. As can be expected, decorrelation from target variability and modeling uncertainty between the channels is a key limitation of this approach.

A number of image restoration and ad hoc enhancement techniques have been developed^{14,47,48,49,58}. An example of an ad hoc technique is simple linear interpolation to increase the pixel density followed by noise addition. The perceptual “resolution” of the interpolated image is improved by adding white noise to the image. This results in the image appearing to have more higher spatial frequency information than is actually supported by the underlying data.

Reconstruction algorithms rely on reconstructing the original signal based on sampled observations. A classic reconstruction algorithm is the well-known Nyquist uniform sampling theorem. Given uniformly-spaced ideal samples of a band-limited signal, the original signal can be exactly reconstructed by ideal low pass filtering of the samples so long as the sample spacing is at least twice the highest frequency present in the signal. Reconstruction algorithms become more complicated with the introduction of irregular sampling and variable apertures, a common problem in microwave remote sensing⁹.

We note that in the signal and image processing literature, the term “image enhancement” generally refers to inverse filtering techniques: to enhance a pre-existing image, an inverse filter is applied by convolution. This approach generally requires a constant (over the image to be processed) aperture function and a pre-existing, uniformly sampled image. The general theory for this approach is well-known^{21,25} and the literature is replete with examples of variations of this method, including techniques to estimate the aperture function from the image. The approach has been successfully applied in remote sensing^{3,4}. As noted, many microwave sensors do not produce data on a uniform grid, and the data must be converted to an image prior to applying such methods. Simple gridded images can be generated with the widely used “drop-in-the-bucket” technique by assigning each measurement to a grid element in which its center falls, or some variation thereof. However, the effective resolution of such images is dictated by the aperture response rather than the grid spacing.

In effect, using reconstruction techniques creates optimal images and performs the function of “image enhancement” at the same time; hence our interest in reconstruction-based techniques. As a result, the remainder of this Chapter focuses exclusively on reconstruction based techniques. Irregular sampling and reconstruction theory are emphasized to support the often non-rectilinear grid sampling of

microwave sensors.

3.1. Microwave Sensor Sampling and Resolution Enhancement

Typical microwave sensor observations can be modeled as an array of samples of spatially filtered surface data. The aperture function for each measurement is defined by the sensor antenna pattern and/or the signal processing techniques used to resolve the antenna illumination pattern into smaller spatial elements, e.g. Doppler filtering or range gating. Spatial sampling is typically obtained via pulsed operation and antenna scanning. While ideally such sampling is on a regular sampling grid, this is not the case for past and present sensors which generally have irregular or varying sampling grids and spatially varying aperture functions. Some sensors (e.g., SASS) can not even be considered ‘imaging sensors’ since the aperture filtered samples do not completely cover the surface for a single pass.

Resolution enhancement algorithms provide improved resolution images by taking advantage of oversampling and the response characteristics of the aperture function to reconstruct the underlying surface function sampled by the sensor. The goal of the algorithm is to generate images from the observations at an effective spatial resolution better than the 3 dB resolution of the sensor; hence the term “resolution enhancement”. When single-pass sampling has inadequate sampling density, multiple observation passes can be combined to improve the sampling density, producing the required oversampled observations for spatial resolution enhancement at the cost of reduced temporal resolution^{3,9,35}.

3.2. Irregular Sampling and Reconstruction

Let $f(x, y)$ represent the true surface image (e.g., σ° or brightness temperature) at a location (x, y) . The measurement system is modeled by

$$z = Hf + \text{noise} \quad (5)$$

where H models the measurement system (including the sample spacing and the system’s spatial response function, hereafter termed the aperture response function) and z is the vector of observations made by the sensor. The measurements z are a discrete sampling of f convolved with the aperture function (which may be different for each measurement). An individual measurement z_i can be written as

$$z_i = \iint h_i(x, y)f(x, y)dxdy + \text{noise} \quad (6)$$

where $h_i(x, y)$ is the aperture response function of the i^{th} measurement. The aperture response is also called the point-spread function. $h_i(x, y)$ is a function of the antenna pattern and the effective signal processing filter response for the i^{th} measurement, see Eqs. (1) and (3).

Reconstruction and resolution enhancement involves inverting Eq. (5)

$$\hat{f} = \hat{H}^{-1}z \quad (7)$$

where \hat{f} is the estimate of f derived from the measurements z . The inverse of H , \hat{H}^{-1} , is exact if H is invertible. If H is not invertible, an approximate solution must be used. The low-pass nature of typical aperture functions passes low spatial frequencies, but attenuates and may even null out higher spatial frequencies. Full reconstruction from sufficiently dense sampling can be considered resolution enhancement since high frequency information suppressed (but not nulled out) by the aperture function is recovered.

Because the sensor measurements are noisy, a tradeoff between resolution enhancement and the noise level in the reconstructed signal exists since high frequency noise tends to be amplified along with the signal in the reconstruction process.

3.3. Sampling and Reconstruction

The traditional approach to sampling and reconstruction is founded on uniform sampling and the well-known Nyquist sampling theorem: a low pass (band limited) function can be completely reconstructed from regularly spaced samples if the sample rate exceeds twice the maximum frequency present in the signal⁴¹. In typical application, signal reconstruction from the samples is accomplished with only a low pass filter and the aperture function is treated as an ideal low pass filter ignored in the reconstruction. For this case, the recovered frequencies are deemed limited to 1/2 the sampling frequency or the cutoff frequency (e.g. the 3 dB rolloff point) of the aperture function, depending on which is lower. The aperture function filters out high frequency components of the signal that might otherwise cause aliasing in the reconstructed signal.

Since the aperture function of a microwave sensor is the result of the antenna pattern and signal processing, it has side lobes. The resulting measurements thus contain information regarding higher frequency components of the original signal. If the (possibly irregular) sampling is sufficiently dense, this information can be recovered by inverting the effects of both the aperture function and the sampling. The reconstruction compensates for the aperture filtering by amplifying attenuated frequencies, though the aperture function may limit the reconstruction due to nulls in its spectrum.

If the sampling is regular (uniform) with a fixed aperture function, reconstruction can be accomplished with low pass filtering and Wiener filtering, a well-known inverse filtering technique that also accounts for noise in the measurements⁴¹ (see, for example, Alvarez-Perez *et al.*¹ for an application of such a technique to ERS scatterometer data). However, inverse filter methods are difficult to apply when the sample spacing is irregular or when the aperture functions vary between different observations. Instead, irregular reconstruction methods must be applied.

While the theory of uniform sampling and reconstruction is well-known, irregular sampling and reconstruction theory is much less familiar. Here we review the general theory for irregular sample reconstruction.

As in uniform sampling, the sample spacing, or *sampling density*, limits the

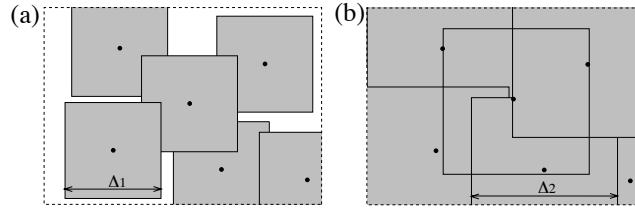


Fig. 2. Graphical illustration of δ -dense in 2-D. A box of size Δ is centered at each sample point. (a) With $\delta = (\Delta_1, \Delta_1)$, the union of the boxes around each sample point is too small to cover the image space. (b) $\delta = (\Delta_2, \Delta_2)$ is sufficiently large. δ -dense corresponds to the smallest δ which covers the full image [from Early and Long (2000)].

signal reconstruction. A simple method for parameterizing the sampling density for an arbitrary irregular grid is based on δ , the maximum sample spacing. A formal definition and discussion of δ -dense sampling is provided in Early and Long⁹; here a less formal approach is adopted. In one dimension, δ specifies the maximal spacing of the samples. In two dimensions δ -dense is defined as the minimum sized rectangle centered at each sample point such that the union of the boxes completely fills the image space (see Fig. 2).

Gröchenig¹⁵ derives a relationship between the sample grid parameter δ and the recoverable frequencies (a band limited frequency range denoted by $\Omega = [\omega_1, \omega_2]$) of the original signal, showing that the signal can be completely reconstructed if

$$\delta \cdot \omega = \sum_{i=1}^2 \delta_i \omega_i < \ln(2). \quad (8)$$

If the spectrum of the original signal has a region of support $\Omega = [-\omega_0, \omega_0]^2$, and the δ -dense sampling grid has $\delta_1 = \delta_2$, the sampling density must satisfy

$$\delta_1 < \frac{\ln(2)}{2\omega_0}. \quad (9)$$

This requires that the minimum irregular sampling density must be higher than the Nyquist uniform sampling density, i.e., $1/\ln(2) \approx 1.44$ times the Nyquist rate for uniformly spaced samples. This ‘oversampling’ is required to ensure reconstruction from the irregular sampling grid.

Thus, for irregular sampling, Gröchenig’s theory is equivalent to the well-known Nyquist theory of sampling and reconstruction for uniform sampling: for complete reconstruction (1) the original signal must be bandlimited or aliasing and information loss results and (2) the sampling must be sufficiently dense. While the original signal can be recovered only if the maximum frequency is less than sampling density, the aperture function used to create the samples can introduce information loss, restricting the frequencies which can be reconstructed.

3.4. Reconstruction Algorithms

Gröchenig's proof is constructive, with an algorithm for reconstructing the original signal from the samples (in effect, inverting H). As demonstrated by Early and Long⁹ Gröchenig's algorithm is equivalent to block additive Algebraic Reconstruction Technique (ART) when used with a suitably defined operator H based on the sampling, the aperture function and the signal bandwidth. ART methods have been extensively studied^{6,12,17} and a number of practical numerical algorithms have been developed. Such methods thus form a basis for the practical reconstruction of irregularly sampled signals in remote sensing.

As previously noted, the sensor observations or measurements can be viewed as ideal samples of an aperture filtered image where the aperture filtered image is the true image convolved with an aperture function. In general, each observation can use a different aperture function. For a given aperture function, nulls in the frequency response of the aperture function result in lost information. For a single aperture, this information is permanently lost and cannot be recovered via reconstruction. However, when multiple aperture functions are used, a net effective aperture function can be defined from the appropriately averaged individual measurement aperture functions⁹. Nulls in the effective aperture function correspond to the intersection of the nulls of individual aperture functions. So long as the sampling density requirements are met for the remaining frequencies, only the frequencies corresponding to the nulls in the net effective aperture function are lost. All other frequencies can be recovered in the reconstruction, subject to the sampling considerations. Though information in spectral nulls of the aperture function is permanently lost, some ART-based reconstruction algorithms can "fill-in" data for missing frequencies based on particular mathematical criteria.

Here we develop the ART algorithm. For convenience the original signal is treated as discrete with uniformly-sized pixels, but at a very fine scale (much smaller than the sample spacing). Each measurement or observation s_i covers a number of these small pixels [compare Eq. (6)]

$$s_i = \sum_j h_{ij} a^j \quad (10)$$

where a^j are elements of the vector a of row-scanned image pixels of the true signal image and h_{ij} is the effective aperture response function for the i th measurement on the j th pixel. The sum is computed over the pixels for which h_{ij} is non-negligible.

Block additive ART (AART) can be written as¹⁷

$$a_{n+1}^j = a_n^j + \frac{\sum_i (s_i - p_i) h_{ij}}{\sum_i h_{ij}} \quad (11)$$

where a_n is the n^{th} iterative estimate of a , and p_i is the back projection

$$p_i = \sum_j h_{ij} a_n^j \quad (12)$$

corresponding to the i th measurement at the n^{th} iteration. In effect, all measurements that cover the pixel of interest are summed and normalized to create the per-pixel update.

The update on the right side of Eq. (11) is a function of the measurement vector s and the back projection vector p computed from the n^{th} iterative estimate. The vector s is the sampled convolution of the true image and the aperture function(s), expressed in matrix form as $s = Ha$ where H (with elements h_{ij}) is the sampled aperture function for each measurement. Then, Eq. (11) becomes (noting $p = Ha_n$)

$$\begin{aligned} a_{n+1} &= a_n + H'(s - p) \\ &= a_n + H'(Ha - Ha_n) \\ &= a_n + \mathcal{H}(a - a_n) \end{aligned} \quad (13)$$

where the a 's are row-scanned image vectors, H' is the row-normalized transpose of H with elements $h_{ji}/\sum_k h_{kj}$. To perform reconstruction consistent with the δ -dense sampling, a low pass filter is applied to the rows of H . The resulting \mathcal{H} is invertible over the frequency range defined by the aperture function and sampling⁹.

As previously noted, noise in the measurements tends to be amplified along with the desired signal. In Wiener filtering, the reconstruction filter response is modified so that when a specified noise-to-signal ratio threshold is exceeded, the response is set to zero to minimize noise amplification²⁵. A similar approach can also be used to modify the rows of H in the reconstruction.

Since the reconstruction algorithm is iterative, computational considerations may limit the number of iterations, resulting in a less-than-optimal reconstruction. Thus, there is a tradeoff between the reconstruction accuracy and resolution and the number of iterations. Increasing iterations improves the resolution. Truncation of the iterations can also be considered a method of regularization²⁵.

In general, iterative reconstruction suffers from two forms of error: reconstruction error and noise amplification. The former is the difference between the iterative image estimate and the noiseless true image. Noise amplification results from the inverse filtering since the reconstruction algorithm acts as a high pass filter. Excess measurements (due to over sampling or repeated observations) contribute to an improvement in the signal to noise ratio of the estimated image due to averaging in the reconstruction algorithm. Thus, increasing the number of measurements improves the noise level, even if the effective sampling density is not increased.

To avoid having to solve for and explicitly compute within the space delineated by the aperture function, regularization techniques can be used to compute a unique solution on the full space. The AART algorithm includes least squares regularization, though a variety of regularization schemes can be applied to generate an estimate of the signal.

As noted by Early and Long⁹ AART and multiplicative ART (MART) solutions differ only by regularization implicit in the algorithms. AART is equivalent to a least squares estimate in the limit based on the minimization of $\|x^2\|$ subject to $y = Hx$

while MART with damping maximizes the signal entropy $-\sum_{j=1}^n x_j \ln x_j$ with the same constraint. The AART estimate is strictly contained within the band limited space defined by the aperture function and sampling, while the MART estimate is not confined to this space – additional frequency content in the null space may be added by the algorithm to create a sharper image²¹, subject to the constraint $y = Hx$. The difference between the AART and MART solutions (in the iteration limit) is contained in the null space of \mathcal{H} .

Alternate variations of these reconstruction algorithms can also be used effectively. The Scatterometer Image Reconstruction (SIR) algorithm is a derivative of MART developed for scatterometer image reconstruction³⁵. It includes a non-linearity in the update to minimize the effects of noise on the reconstruction and is preferred over MART^{9,58}. The SIR algorithm has been widely applied to both scatterometer and radiometer data^{29,31,35}. When applied to scatterometer data, the multivariate form of SIR estimates the incidence angle dependence of the scatterometer data³⁵ and is used below. Another reconstruction approach is based on the Backus-Gilbert technique^{13,46,52,53}, contrasted with SIR by Long *et al.*³¹.

While the overall performance of AART, MART and SIR algorithms are similar, at lower reconstruction errors MART and SIR have lower noise amplification than AART, and at the lowest reconstruction errors, SIR has the lowest noise. Thus, SIR is more robust in the presence of noise, particularly at low signal to noise ratios⁹. Further, the subjective image quality for SIR at a given reconstruction error level is better than corresponding MART or AART products when used with scatterometer data. The ultimate limits to resolution enhancement are the sampling density, nulls introduced by the aperture function(s), the acceptable noise level, and the temporal stability of the study area^{9,35}. Inverse filtering of the reconstructed SIR image can further improve the quality of the image⁷.

4. Application Example: ESCAT Resolution Enhancement

As has been noted, reconstruction-based resolution enhancement is based on restoring attenuated information in the sidelobes of the spatial response function within the support of the sampling. High side lobes in the spatial response make this easier, though information can be recovered even from sensors with low sidelobes. To illustrate this we consider a particular application example: ESCAT, which uses a processing window designed to minimize sidelobes. ESCAT also has a much narrower swath than other sensors and thus requires many more passes over the target to achieve a similar high sampling density. Application of resolution enhancement techniques to ESCAT is thus more demanding than for other scatterometers^{9,10,29,35}.

For ESCAT, ground processing is used to spatially filter and resample the raw instrument measurements. Several pulses corresponding to each along-track cell are integrated into a single “50 km” resolution measurement. Nominally 50 km σ° measurements are reported on a 25 km grid for each antenna. A spatial smoothing filter (Hamming window) is applied when integrating the pulses. This filter smoothes the

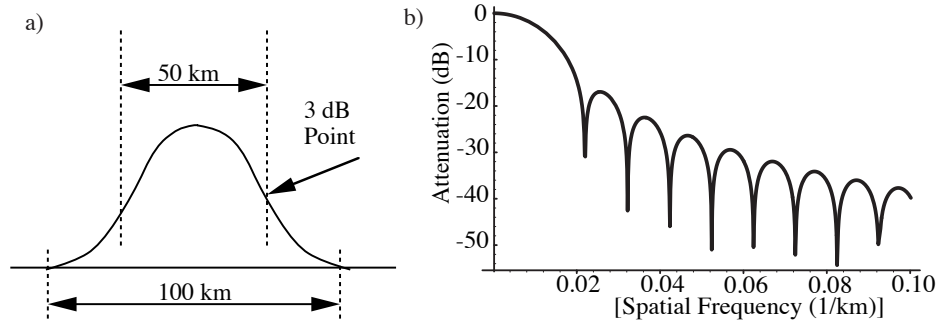


Fig. 3. a) Plot of the ESCAT response along a section of the spatial resampling filter. b) Spatial spectrum of a).

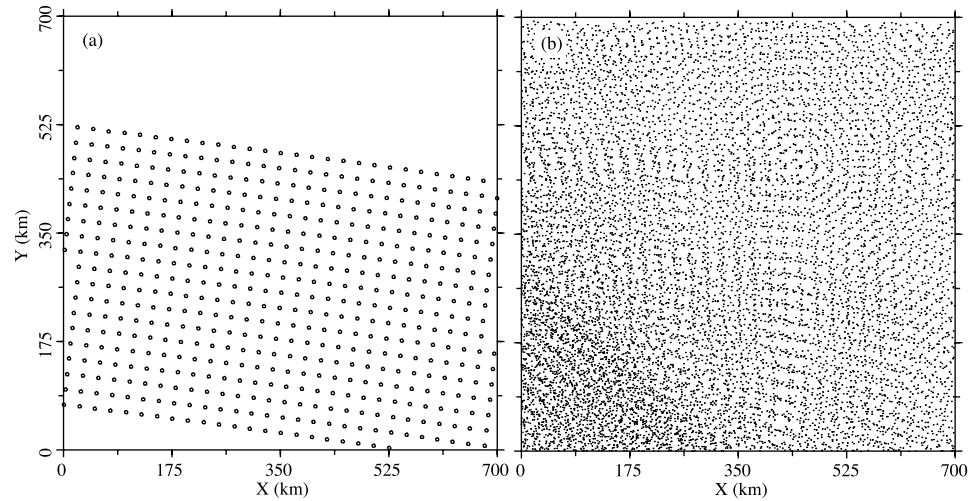


Fig. 4. a) Locations of the σ^0 measurement centers for a single pass over a small study area. b) Locations of the σ^0 measurement centers over a 6 day period.

σ^0 response so that it corresponds to the average σ^0 response for a 50 km circle (see Fig. 3)^b. This weighting function, chosen to minimize sidelobes and aliasing, is the primary factor in determining the effective measurement response or aperture function. The windowed spatial resampling has the desirable dual effects of 1) reducing the noise level (i.e., decreasing K_P and improving the radiometric resolution) and 2) compensating for the varying areas and resolutions of the individual measurements. For each 25 km grid element there are three measurements of σ^0 , one from each antenna beam. In many land and ice applications these may be combined; however, care must be used for surfaces exhibiting azimuthal variation in σ^0 .

^bE. Attema, Personal communication.

Based on the Nyquist theorem, frequencies up to 0.02 km^{-1} ($1/50$) can be reconstructed from uniform 25 km sampling. If multiple passes over a given study region are combined, the effective sampling density can be improved. Combining multiple passes results in a dense, but irregular sampling grid. For example, Fig. 4a illustrates the ESCAT measurement locations for a single pass over a particular study area. These are on a 25 km uniformly spaced sampling grid. Figure 4b shows the locations of all measurements collected over the study area in a 6 day period. Note that NSCAT and SeaWinds achieve significantly denser sampling during a similar period⁹ (see also Fig. 1). Of course, in order to usefully combine the multiple passes to achieve the dense sampling the following assumptions must be made: 1) the instrument calibration is stable, 2) the surface σ° remains essentially constant for the combination period, 3) the surface σ° does not vary with azimuth angle since different passes may observe the surface at different azimuth angles, and 4) the location and response function(s) of the measurements are accurately known³⁵.

To address these considerations we note that both ERS-1 and ERS-2 scatterometers have demonstrated excellent calibration stability³², satisfying assumption 1. Applying assumption 2 limits the multiple pass combination technique to stationary or very slowly evolving targets such as land¹⁰; ocean or rapidly moving sea ice regions are unsuited for combining multiple passes. Assumption 3 can be applied for much of the Earth's surface, although there are known regions of Antarctic glacial ice which exhibit significant azimuth dependence in C-band σ° ^{11,19,26,27,28,45} and caution must be exercised in such cases. Given care in the implementation of the ground processing of the ESCAT data, assumption 4 is reasonable.

Proper reconstruction involves inverting the effects of the sampling and aperture function (i.e. the resampling window for ESCAT) over the frequency range supported by the sampling. Windowing introduces nulls in the measurement spectra (see Fig. 3) and at such frequencies the original signal cannot be recovered. However, over frequencies supported by the sampling at which the signal spectra is merely attenuated, the original signal can be completely recovered: the reconstruction algorithm can compensate for the attenuation introduced by the resampling filter—even in the highly attenuated sidelobe regions. Simulations demonstrate that sidelobe compensations of over 60 dB are possible using SIR with this aperture, sufficient sampling, and long enough iteration.

We note that the original SIR algorithm was developed for SASS where the aperture function could be approximated by a boxcar or rect function, simplifying the algorithm³⁵. However, for the SSM/I and ESCAT it is appropriate to use the actual response function in the SIR algorithm. As a general rule, the lower sidelobes of the ESCAT aperture function require more iterations to achieve the same level of resolution enhancement compared to more rect-like aperture functions.

The noise performance of SIR can optionally be improved via use of a median filter, a modification known as SIRF (SIR with Filtering)³⁵; however, this has the side effect of reducing the effective resolution. SIRF was used with SASS measure-

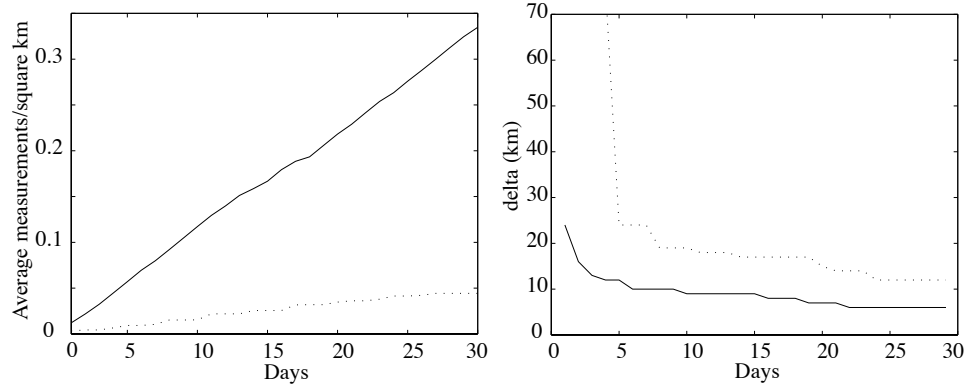


Fig. 5. a) Plot of δ -dense versus time for two study areas. b) Average number of σ° measurements per square km as a function of time for two locations. In both plots the solid line is for a polar location while the dotted line corresponds to an arbitrary mid-latitude location.

ments due to their high noise level. ESCAT measurements are much less noisy than SASS measurements due to the better SNR and so the median filter is not used with ESCAT. A previous author⁵⁶ erroneously stated that resolution enhancement can not be applied to ESCAT data due to the windowing applied in the measurement process. However, as we have shown the windowing primarily only degrades the signal to noise ratio and information in even very low sidelobes can be recovered if desired and the noise enhancement can be tolerated. The same author attributed the resolution enhancement of SIR to the use of a median filter; however, SIR does not include a median filter. The primary limitations of ESCAT resolution enhancement are the degradation of the signal to noise ratio and the computational time, which limits the number of iterations.

4.1. Sampling Density

We now consider the sampling density achievable for ESCAT. Combining multiple passes increases the sampling density, quantified by δ . However, due to the ERS orbit and swath geometry, the number of passes in a given time period and their relative orientation and spacing varies considerably over different regions of the Earth. Further, since the scatterometer mode can not be used when SAR data is being collected, there are gaps and missing data. In any case, the multi-orbit sampling is suboptimum. Nevertheless, as the number of overpasses is increased, δ decreases in a location-dependent manner. To illustrate the relationship between the δ parameter and time, Fig. 5 plots δ computed over two study regions, one at mid latitudes in the Northern Hemisphere and the other in the polar region, which gets more frequent coverage. The value of δ and the average number of measurements per square km are both shown. A tradeoff between δ and time is apparent. There is a general linear trend in the number of measurements while δ exhibits an

exponential decay with time. We note that the reconstruction resolution limit is approximately $2.9 \times \delta$ (see Eq. 9). Because of concerns about temporal variations in the surface, we desire to minimize the temporal period of the measurements to be combined. However, to achieve a given sampling density (and therefore resolution in the resulting reconstructed image), a minimum time interval is required, termed the ‘imaging period.’

It should be clear that the selection of the imaging period depends on the intended application. However, the point of inflection in the δ versus time curve provides a good tradeoff between length of the imaging period and sampling density. Examining Fig. 5 we see that six days provides a δ of 10 km (corresponding to an effective reconstruction resolution of approximately 29 km) for the polar region while nearly a month is required for the particular mid latitude region evaluated. For the same period a δ of approximately 6 km near the poles is achieved. Higher density sampling is possible but requires longer time periods.

We note that δ is dependent on the *worst-case* sample spacing over the study area, which may occur at only one point; the sample density elsewhere is higher. While δ -dense defines the sample spacing required to guarantee the reconstruction resolution everywhere, regions of the image with denser sampling can yield higher enhancement in practice due to locally denser sampling. For example, the area covered by a single pass has a δ of 25 km, even if the remainder of the image area is not covered at all. (This explains the high starting value of δ in Fig. 5.) Thus, the reconstructed resolution can vary over the image.

4.2. Simulated Performance

To illustrate the application of SIR to ESCAT measurements, simulation is initially used. In the simulation, the geometry and response function from actual ESCAT measurements over a small study region in Antarctica are used with synthetic \mathcal{A} and \mathcal{B} “truth” images (see Fig. 6) to generate simulated σ° measurements. Monte Carlo noise with the expected ESCAT K_p is added to the measurements. The synthetic images include a number of features to aid in evaluating the resolution enhancement including various width lines, a pyramid feature and two small, closely spaced squares. The squares are approximately 25 km in size and spaced 25 km apart. We note that the synthetic images are not bandlimited (as is required by reconstruction theory). This enables us to evaluate the effects of attempting to reconstruct a non-bandlimited image.

The result of applying the SIR algorithm is shown in Fig. 6. The pixel resolution used in these images is 4.45 km. The effective resolution is, of course, less than the pixel resolution. The results after 30 and 100 iterations of the SIR algorithm are shown when 6 days and 30 days of data are used. For comparison, nonenhanced ESCAT images with a pixel resolution of approximately 25 km (5×4.45 km) are also shown. To generate the nonenhanced images, all measurements whose center falls within a given pixel are used to estimate \mathcal{A} and \mathcal{B} using linear (in dB) regression.

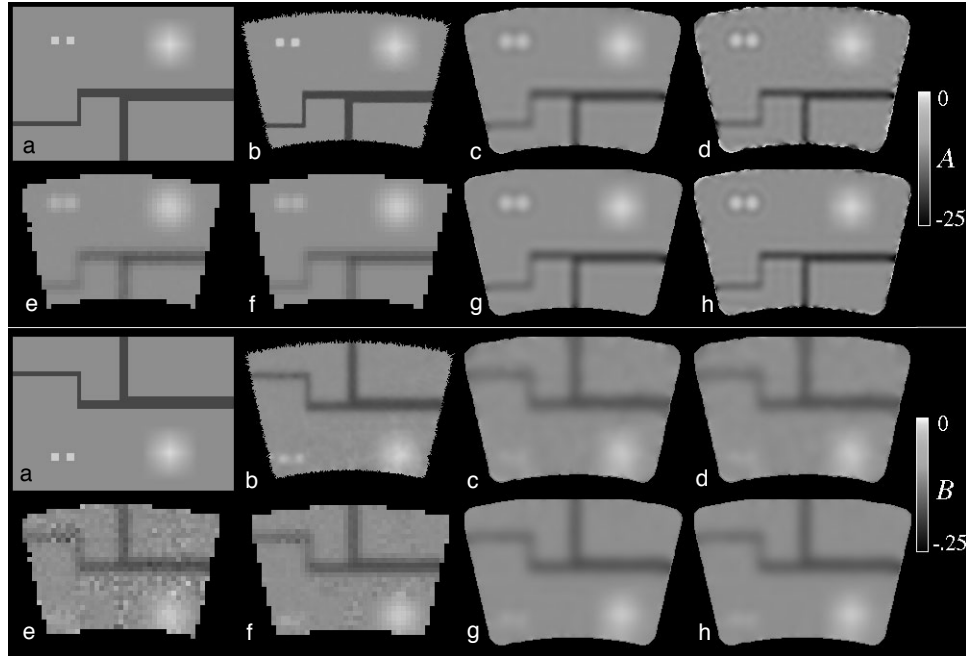


Fig. 6. ESCAT resolution enhancement simulation results. The pixel resolution is 4.45 km. The upper panel contains \mathcal{A} images while the lower panel contains \mathcal{B} images. The subimages in each panel are: a) true synthetic image, b) simulated NSCAT SIR result, c) simulated ESCAT result for 30 iterations with 6 days of data, d) simulated ESCAT result for 1000 iterations with 6 days of data, e) nonenhanced (see text) results for 6 days, f) non-enhanced for 30 days of data, g) simulated ESCAT result for 30 iterations with 30 days of data, and h) simulated ESCAT result for 1000 iterations with 30 days of data.

For ease of display and comparison, each pixel of the nonenhanced images was replicated five times in each direction to expand its size to match the equivalent area of the other images. Also shown are NSCAT comparison images, the result of SIRF processing 6 days of synthetic NSCAT measurements generated in a manner similar to the synthetic ESCAT measurements. The NSCAT images use 50 iterations of SIRF⁴⁴.

Examining Fig. 6 we note that the NSCAT image has better resolution than the ESCAT image. Due to the lower sidelobes of ESCAT data, the improvement in the ESCAT resolution is lower than NSCAT for the same number of iterations. The effective resolution of the ESCAT images improves for both increasing iterations and also when more measurements are incorporated. As more measurements are included, the noise level in the images drops. Also, the SIRF-processed images are subjectively better than the nonenhanced images both in terms of resolution and noise level. Careful examination reveals low amplitude artifacts due to low pass filtering of the true image in all of the enhanced resolution images. This effect will be discussed in greater detail later. We note that the \mathcal{B} images exhibit somewhat

lower resolution than the \mathcal{A} images, an effect previously noted³⁵.

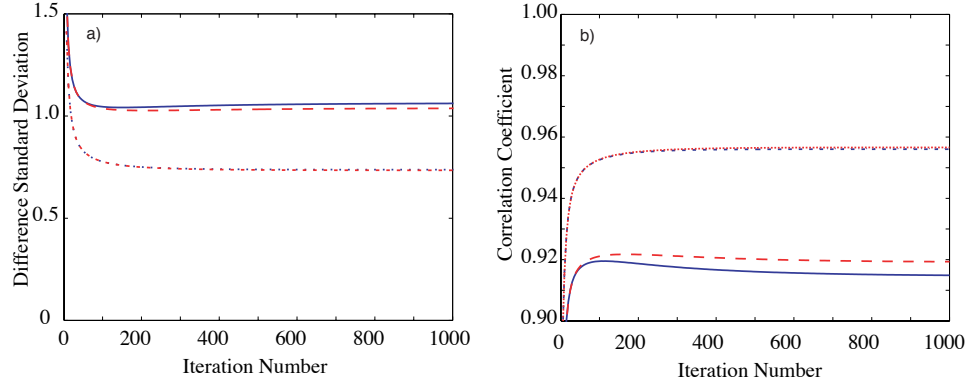


Fig. 7. a) Plot of the standard deviation of the difference between the images versus iteration number. b) Plot of the correlation coefficients of the images version iteration number. In both plots the solid line is the true-ESCAT 6 day image, the long dash line is the true-ESCAT 30 day image, the short dash line is the 6 day ESCAT-NSCAT, and the dotted line is the 30 day ESCAT-NSCAT. In a) the latter two lines lie nearly on top of each other and can not be distinguished in this plot.

To objectively quantify the resolution enhancement, we compare the error between the ESCAT and true images and, to gain insight with later comparisons of actual data, with NSCAT images. As a metric, we compute the standard deviation of the difference of the respective images. We also compute the correlation coefficients. These metrics are computed for the \mathcal{A} images as a function of the iteration number in Fig. 7. After an initially steep decrease, the ESCAT-true standard deviation of the 6 day measurement set bottoms out at about 75 iterations and begins a slow rise. The ESCAT-true 30 day set is similar, with a much slower rise and a minimum at about 200 iterations. The ESCAT-NSCAT standard deviation for both the 6 day and 30 day cases, look similar, though lower and with a minima at approximately 500 iterations. The correlation coefficient exhibits a behavior consistent with the standard deviation, with a rapid initial increase in correlation, a peak and then a gradual decrease in the correlation. The minima for the ESCAT-true correlation is at approximately 100 and 150 for the 6 day and 30 day cases, respectively. For ESCAT-NSCAT, the peak is at 500 iterations.

Detailed examinations of the images and their spectra at each iteration (not shown) suggest that the initial standard deviation decrease and correlation increase are due primarily to the recovery of the signal in the main lobe of the aperture function response. As the iterations continue, the difference between the reference signal and the image decreases. The image component due to the noise begins small and gradually increases with iteration. Eventually, the increasing noise begins to dominate over the decreasing signal error, leading to the increase in standard deviation and decrease in correlation. Consideration of the sensitivity of the particular

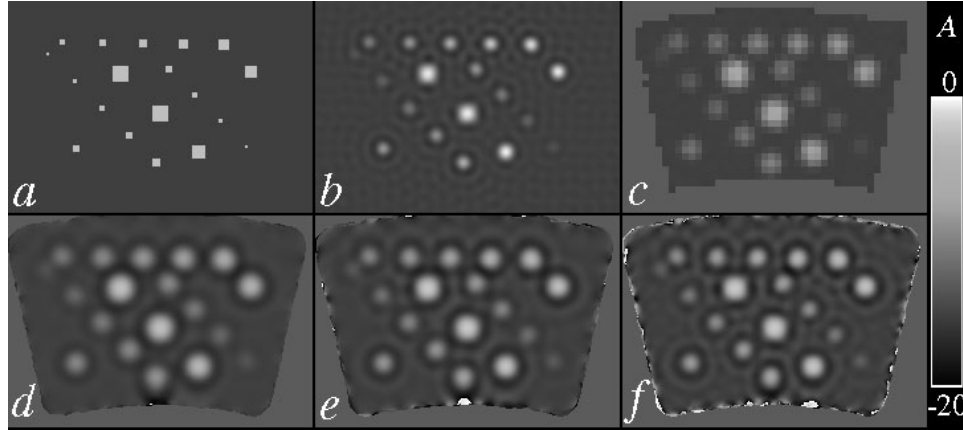


Fig. 8. \mathcal{A} image comparison using six days of data. Actual measurement locations over a small polar region are used to create noisy synthetic σ° measurements of the true image. a) True synthetic \mathcal{A} image containing variously sized targets. b) True image low pass filtered to 25 km resolution. Note ringing artifacts due to the low pass filter. c) Non-enhanced resolution image (see text). d) Result after 30 iterations of SIR. e) Result after 100 iterations of SIR. f) Result after 840 iterations of SIR.

application of the image data dictates the level of noise enhancement that can be tolerated and hence the resolution enhancement. The available computational resources may also be a factor, particularly for large images. While more iteration leads to better resolution, it also increases the noise level which is the primary limitation for ESCAT enhancement.

To better understand the tradeoff between resolution and the number of iterations, the results of a second simulation are shown in Fig. 8. Only the \mathcal{A} images are shown. The simulation procedure is identical to the previous one but with a different synthetic image. Six days of data are used (though as could be expected, better results are obtained with 30 days of data). The synthetic image (Fig. 8a) contains a set of different sized boxes to aid in the evaluation of the resolution of the resulting images. The boxes range in size from 8.9 to 71 km. Along the top row the boxes increase from 17.8 km to 35.6 km. The simulated σ° measurements are generated from this image. A lowpass filtered version of the true image is shown in Fig. 8b. This reflects an ideally reconstructed image using an ideal lowpass filter with a cutoff at 25 km. For reference Fig. 8c shows the corresponding nonenhanced \mathcal{A} image. Figures 8d-f show the results of SIR after 30, 100, and 840 iterations. The bright edge around the SIR images is a simulation artifact. The increasing sharpness of the SIR images with increasing iteration is apparent.

While the larger diameter of the dark rings for the SIR images initially suggests that the resolution is not as good as the lowpass filtered true image, examination of the 3 dB widths of the boxes in the image estimates suggests otherwise. Figure 9 plots the \mathcal{A} values in the images in Fig. 8 along a line through the top row of boxes.

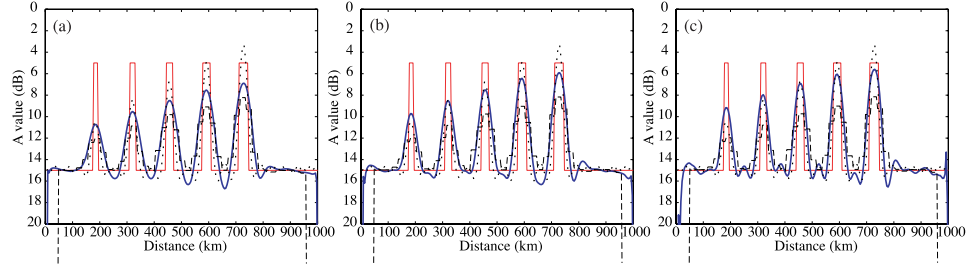


Fig. 9. Plot of \mathcal{A} values extracted from the images in the previous figure across the top row of spots. The light solid line is the true image. The dark solid line is the SIR estimate. The dotted line is the 25 km low-pass filtered true image. The dashed line is the nonenhanced image data. a) 30 iterations. b) 100 iterations. c) 840 iterations.

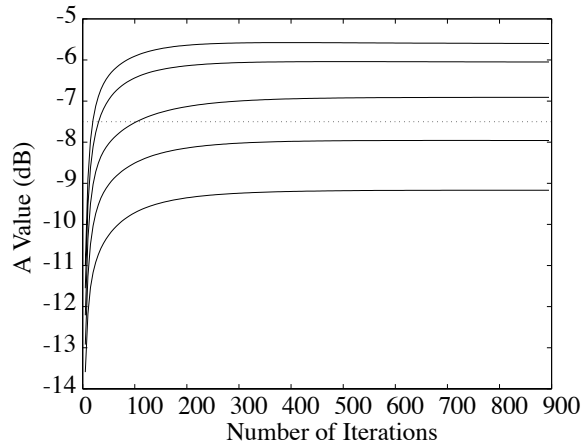


Fig. 10. Plot of the peak \mathcal{A} value in the SIR image over each of the top row of squares as a function of the number of iterations. The dotted line is at -7.5 dB, the 3 dB point.

Three plots are shown, one for each SIR iteration count considered. In these plots the dark solid line is the SIR image estimate while the dotted line is the lowpass filtered true image. Comparing the three plots, the adaptation of the SIR image with iteration is apparent. Examining the SIR plot and the lowpass filtered plot, it can be seen that the box peaks for SIR are above the lowpass peaks for small objects and somewhat below for large objects. The closest overall match occurs for 100 iterations. Figure 10 plots the heights of each of the boxes as a function of iteration. The dotted line corresponds to the 3 dB point. Thus, using a 3 dB effective resolution criterion, we conclude that the smallest resolvable box for 6 days of data and 100 iterations is approximately 25 km. However, smaller features are more readily apparent (as a larger peak) than predicted by the lowpass filtered image suggesting that there is, in fact, information at higher frequencies than this. Further, as the algorithm is iterated longer, the effective resolution continues to

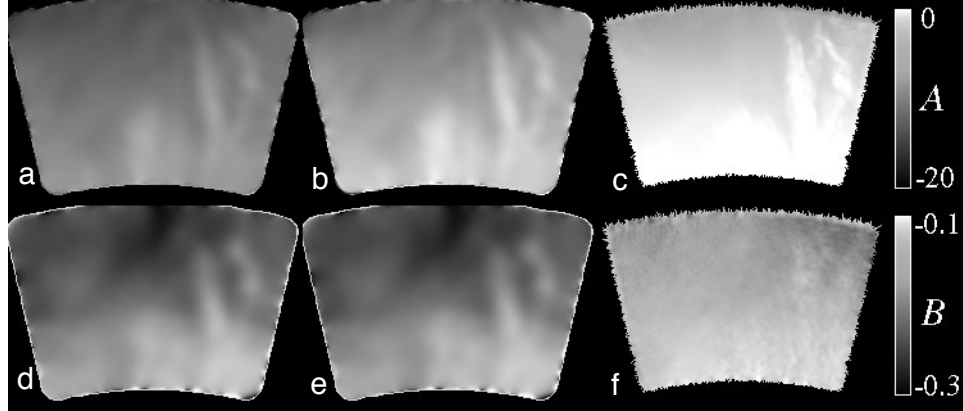


Fig. 11. \mathcal{A} image resolution enhancement results for actual data over a small study region in Antarctica. The pixel resolution is 4.45 km. a) ESCAT \mathcal{A} result for 35 iterations, b) ESCAT \mathcal{A} result for 1000 iterations. c) NSCAT \mathcal{A} result. d) ESCAT \mathcal{B} result for 35 iterations, e) ESCAT \mathcal{B} result for 1000 iterations. f) NSCAT \mathcal{B} result.

improve, albeit slowly. Based on these simulations, it is possible to obtain enhanced resolution images from ESCAT measurements even for short imaging periods.

4.3. Actual Data

Having used simulation to evaluate the resolution enhancement of ESCAT data, actual data is now considered. One of the difficulties with using actual data is that the true values of \mathcal{A} and \mathcal{B} are not known, making a quantitative evaluation of the resolution enhancement very difficult. Instead, we compare the enhanced resolution images to data from other sensors. This comparison is complicated by the fact that sensors operate at different frequencies and so the surface response characteristics vary. Nevertheless with this limitation in mind, the correlation between the sensors can provide a measure of the resolution enhancement. Two study regions are considered: polar (Antarctica) and mid-latitude (Amazon).

In the polar region example, 6 days of data are used to generate \mathcal{A} and \mathcal{B} images of Wilkes land in Antarctica. The results are shown in Fig. 11 for two different SIR iterations. An NSCAT-derived image of the same location and time is shown. Plots of the ESCAT-NSCAT standard deviation and correlation are shown in Fig. 12. We note that ESCAT and NSCAT operate at different frequencies (5.6 GHz versus 14.0 GHz) which can be expected to have somewhat different responses to surface features. Nevertheless, similar features are observed in the \mathcal{A} images from both sensors, with the ESCAT images appearing like lowpass versions of the NSCAT images. Greater differences are evident in the \mathcal{B} images. While this is not well-understood, it may be due to the differences in scattering at different frequencies from interannual layers in the Antarctic firn or azimuth modulation of the backscatter with azimuth angle. Careful examination of the ESCAT \mathcal{A} images reveals somewhat sharper edges

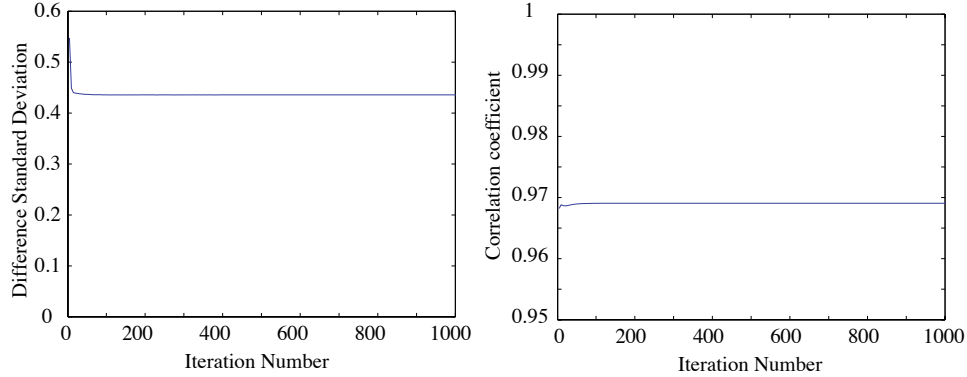


Fig. 12. a) Plot of the standard deviation of the difference between the ESCAT and NSCAT \mathcal{A} image results versus iteration number. b) Plot of the correlation coefficient between the ESCAT and NSCAT \mathcal{A} image results versus iteration number.

on the features in the image resulting from more iterations, suggesting higher effective resolution. As in the simulations, the ESCAT-NSCAT standard deviations and correlations show rapid initial improvement, more gradual improvement, a minimum and then very gradual degradation with iteration due to noise enhancement.

For the Amazon region, a small study region covering part of the Amazon river is considered. Non-enhanced and resolution enhanced images from ESCAT, NSCAT, and SeaWinds data are compared in Fig. 13. This image compares the output of both the SIR and AVE algorithms. The AVE algorithm³⁵ is defined as the first iteration of SIR. In this example, images from both types of SeaWinds measurements are shown. SIR with the actual antenna response was used with SeaWinds 25 km 'egg measurements' while SIRF was used on SeaWinds 6×25 km 'slice measurements'. SIRF was also used for NSCAT. For this comparison the number of iterations was limited to 30 for SIR and 50 for SIRF. Again, note that additional iteration improves the resolution, but also increase the noise. However, this comparison restricts the number of iterations to a small number. The imaging period varies from 4 days for SeaWinds to 6 days for ESCAT and NSCAT. The pixel resolution is 4.45 km. Examining these images it is apparent that SIR yields improved resolution images compared to both AVE and non-enhanced. While the resolution improvement for ESCAT is less than the other sensors, ESCAT resolution enhancement is effective.

5. Conclusion

This Chapter has considered spatial resolution enhancement by reconstruction from irregularly sampled microwave sensor observations. Given sufficiently dense sampling, an enhanced resolution image of the surface can be generated using reconstruction from the sensor observations. In the resulting image the attenuation resulting from effective aperture function is compensated for, exclusive of the spectral nulls in the effective aperture function. The aperture function arises from the net

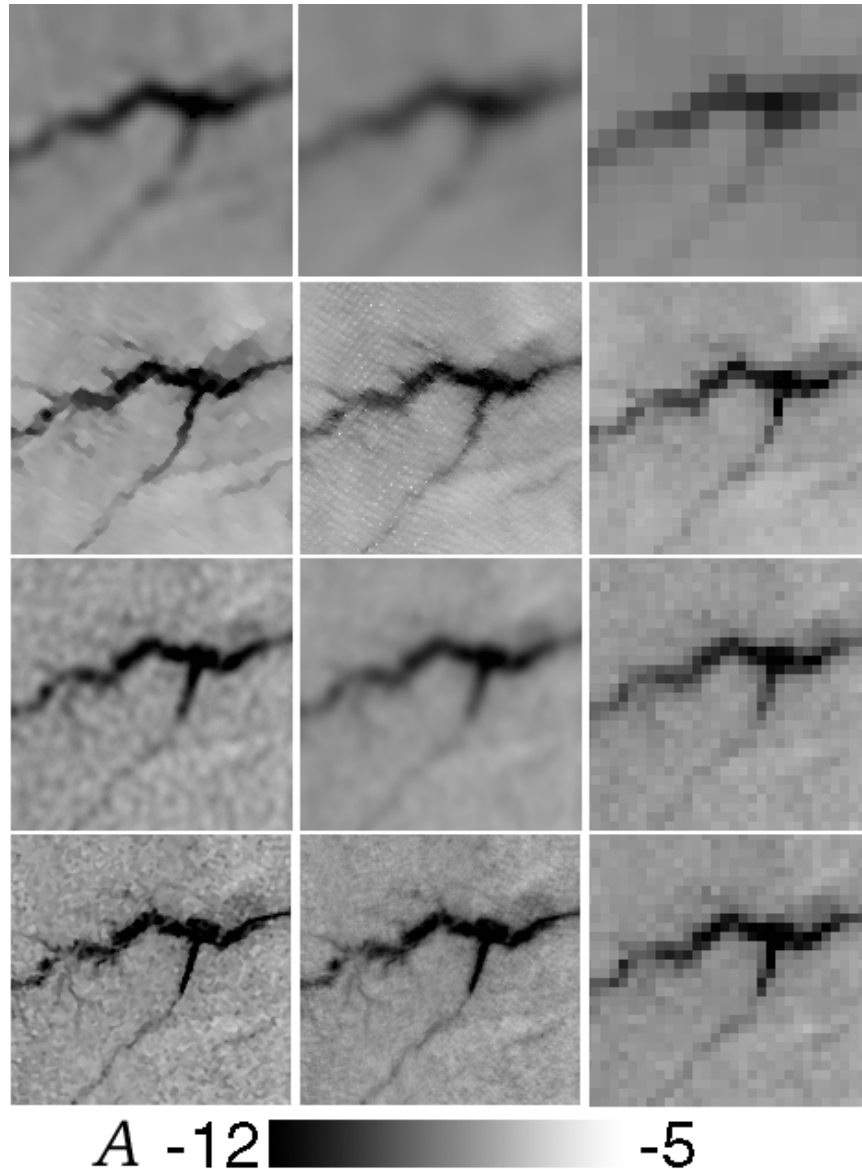


Fig. 13. Comparison of enhancement results over the Amazon. Columns are, left to right, SIR-enhanced, AVE-enhanced, and non-enhanced. Rows are, top to bottom, ESCAT, NSCAT, SeaWinds Eggs, and SeaWinds Slices. ESCAT is at C-band, while the others are Ku-band. SeaWinds images are H-pol, 46° incidence angles. All other images are V-pol, 40° incidence angle. SIR iteration is limited to 30 while SIRF iteration is limited to 50 in these images.

effect of the antenna pattern and any signal processing involved in generating the measurements, and may be different for different measurements. Reconstruction inverts both the aperture and sampling. Resolution enhancement relies on retriev-

ing high frequency information attenuated by the aperture function in oversampled data. The enhancement is limited by nulls in the aperture function and the sampling density. Noise enhancement in the reconstruction can also be a limiting factor. When required, the sample density can be increased by combining data from multiple passes, at the expense of temporal averaging and reduced temporal resolution. The reconstructed images have “enhanced resolution” since the effective resolution can be much finer than the nominal 3 dB sensor resolution. Additive and multiplicative ART can be used as reconstruction algorithms, though the derivative SIR algorithm is more robust in the presence of noise. SIR has been successfully applied to scatterometer and radiometer data^{9,29,31,35}.

As an illustration, the technique is applied to ESCAT data, which is a very demanding application due to the windowed aperture function in the data. Tradeoffs for ESCAT are considered and SIR is shown to improve the resolution of the ESCAT data when multiple orbits are combined. ESCAT results are compared to NSCAT and Seawinds.

References

1. J.L., Alvarez-Perez, S.J. Marshall, and K. Gregson, Resolution Improvement of ERS Scatterometer Data Over Land by Wiener Filtering, *Remote Sens. Environ.*, **71**, pp. 261–271, 2000.
2. E. Attema, The Active Microwave Instrument Onboard the ERS-1 Satellite, *Proc. IEEE*, **79**, 6, pp. 791–799, 1991.
3. B.G. Baldwin, W.J. Emery, and P.B. Cheeseman, Higher Resolution Earth Surface Features from Repeat Moderate Resolution Satellite Imagery, *IEEE Trans. Geosci. Remote Sens.*, **36**, 1, pp. 244–255, 1998.
4. C. Byrne, *et al.*, Image Restoration and Resolution Enhancement, *J. Opt. Soc. Am.*, **73**, 11, pp 1481–1487, 1983.
5. B. Caccin, C. Roberti, P. Russo, and A. Smaldone, The Backus–Gilbert Inversion Method and the Processing of Sampled Data, *IEEE Trans. Signal Process.*, **40**, pp. 2823–2825, 1992.
6. Y. Censor, Finite Series-Expansion Reconstruction Methods, *Proc. IEEE*, **71**, 3, pp. 409–419, 1983.
7. W.B. Davis, *Enhanced Resolution Imaging from Remotely Sensed Microwave Data*, Masters Thesis, Brigham Young University, 1983.
8. J.E.H. Dyal, *TRMM Sigma-0 Vegetation Signatures and Other Studies*, Masters Thesis, Brigham Young University, 1999.
9. D.S. Early and D.G. Long, Image Reconstruction and Enhanced Resolution Imaging From Irregular Samples, *IEEE Trans. Geosci. Remote Sens.*, **39**, 2, pp. 291–302, 2001.
10. D.S. Early and D.G. Long, Error Characteristics of the SIR Resolution Enhancement Algorithm, *Proc. Int. Geosci. Rem. Sens. Sym.*, pp. 124–126, Lincoln, Nebraska, 27–31 May, 1996.
11. D.S. Early and D.G. Long, Azimuth Modulation of C-band Scatterometer sigma-0 Over Southern Ocean Sea Ice, *IEEE Trans. Geosci. Remote Sens.*, **35**, 5, pp. 1201–1209, 1997.
12. T. Elfving, On Some Methods for Entropy Maximization and Matrix Scaling, *Linear Algebra and its Applications*, 34, pp. 321–339, 1980.

13. M.R. Farrar and E.A. Smith, Spatial Resolution Enhancement of Terrestrial Features Using Deconvolved SSM/I Brightness Temperatures, *IEEE Trans. Geosci. Remote Sens.*, **30**, 2, pp 349–355, 1992.
14. P. Gagne and H.H. Arsenault, Using Information from Multiple Low-Resolution Images to Increase Resolution, *Proc. of SPIE*, **1564**, pp 656–663, 1991.
15. K. Gröchenig, Reconstruction Algorithms in Irregular Sampling, *Mathematics of Computation*, **59**, 199, pp. 181–194, 1992.
16. N.C. Grody, Classification of Snow Cover and Precipitation Using the Special Sensor Microwave/Imager, *J. Geophys. Res.*, **94**, pp. 7423–7435, 1991.
17. P. Gilbert, Iterative Methods for the Three-Dimensional Reconstruction of an Object from Projections, *J. Theor. Bio.*, **36**, pp. 105–117, 1972.
18. J.P. Hollinger, J.L. Pierce, G.A. and Poe, SSM/I Instrument Evaluation, *IEEE Trans. Geosci. Remote Sensing*, **28**, 5, pp. 781–790, 1990.
19. G. Hyland and N. Young, Wind-induced directional anisotropy of microwave backscatter and its impact on imaging of the Antarctic continental snow cover, *Proc. Int. Geosci. Rem. Sens. Sym.*, pp. 1988–1990, 1998.
20. T.J. Jackson and T.J. Schmugge, Algorithm for the Passive Microwave Remote Sensing of Soil Moisture, in *Microwave Radiometry and Remote Sensing Applications* (P. Pampaloni, ed.), (Zeist), pp. 3–17, VSP, 1989.
21. A.K. Jain, *Fundamentals of Digital Image Processing*, Prentice Hall, Englewood Cliffs, NJ, 1989.
22. A.S. Jones and T.H.V. Haar, Passive Microwave Sensing of Cloud Liquid Water Over Land Regions, *J. Geophys. Res.*, **95**, pp. 16673–16683, 1990.
23. W.L. Jones, L.C. Schroeder, D.H. Boggs, E.M. Bracalente, R.A. Brown, G.J. Dome, W.J. Pierson, and F.J. Wentz. The SEASAT-A Satellite Scatterometer: The Geophysical Evaluation of Remotely Sensed Wind Vectors Over the Ocean. *J. Geophys. Res.*, **87**, C5, 3297–3317, 1982.
24. T. Kawanishi, H. Takamatsu, T. Kosu, K. Okamoto, H. and Kumagai, TRMM Precipitation Radar, *Proc. IGARSS'93*, pp. 423–425, Tokyo, Japan, Aug., 1993.
25. R.L. Lagendijk and J. Biemond, *Iterative Identification and Restoration of Images*, Kluwer Academic Publishers, Boston, 1991.
26. P. Lecomte, A. Cavanie, and F. Gohin, Recognition of Sea Ice Zones using ERS-1 Scatterometer Data, *Proc. Int. Geosci. Rem. Sens. Sym.*, pp. 855–857, 1993.
27. M. Ledroit, F. Remy, and J.F. Minster, Observation of the Antarctic ice sheet with the Seasat Scatterometer: relation to katabatic wind intensity and direction, *J. Glaciology*, **39**, 132, pp. 385–396, 1993.
28. D.G. Long and M.R. Drinkwater, Azimuth Variation in Microwave Scatterometer and Radiometer Data Over Antarctica, *IEEE Trans. Geosci. Remote Sens.*, **38**, 4, pp. 1857–1870, 2000.
29. D.G. Long and M.R. Drinkwater, Cryosphere Applications of NSCAT Data, *IEEE Trans. Geosci. Remote Sens.*, Vol. 37, 3, pp. 1671–1684, 1999.
30. D.G. Long, Comparison of TRMM and NSCAT Observations of Surface Backscatter Over the Amazon Rainforest, *Proc. Int. Geosci. Rem. Sens. Sym.*, pp. 1879–1881, Seattle, Washington, 6–10 July, 1998.
31. D.G. Long and D. Daum, Spatial Resolution Enhancement of SSM/I Data, *IEEE Trans. Geosci. Remote Sens.*, **36**, pp. 407–417, 1997.
32. D.G. Long and G.B. Gkouson, Calibration of Spaceborne Scatterometers Using Tropical Rainforests, *IEEE Trans. Geosci. Remote Sens.*, **34**, 2, pp. 413–424, 1996.
33. D.G. Long and P. Hardin, Vegetation Studies of the Amazon Basin Using Enhanced Resolution Seasat Scatterometer Data, *IEEE Trans. Geosci. Remote Sens.*, **32**, 2,

- pp. 449–460, 1994.
34. D.G. Long and M.R. Drinkwater, Greenland Observed at High Resolution by the Seasat-A Scatterometer, *J. Glaciology*, **32**, 2, pp. 213–230, 1994.
35. D. Long, P. Hardin, and P. Whiting, Resolution Enhancement of Spaceborne Scatterometer Data, *IEEE Trans. Geosci. Remote Sens.*, **31**, pp. 700–715, 1993.
36. D.G. Long and J.M. Mendel, Identifiability in Wind Estimation from Wind Scatterometer Measurements, *IEEE Trans. Geosci. Remote Sensing*, **29**, 2, pp. 268–276, 1991.
37. M.J. McFarland, R.L. Miller, and C.M.U. Neale, Land Surface Temperature Derived From the SSM/I Passive Microwave Brightness Temperatures, *IEEE Trans. Geosci. Remote Sensing*, Vol. 28, pp. 839–845, 1990.
38. F. Naderi, M.H. Freilich, and D.G. Long, Spaceborne Radar Measurement of Wind Velocity Over the Ocean—An Overview of the NSCAT Scatterometer System, *Proc. IEEE*, **79**, 6, pp. 850–866, 1990.
39. E.G. Njoku, J.M. Stacey, and F.T. Barath, The Seasat Scanning Multichannel Microwave Radiometer (SMMR): Instrument Description and Performance, *IEEE J. Ocean. Eng.*, **EO-5**, No. 2, pp. 100–115, 1980.
40. W.S. Olson, C-L Yeh, J.A. Weinman, R.T. Chin, Resolution Enhancement of Multichannel Microwave Imagery from the Nimbus-7 SMMR for Maritime Rainfall Analysis, *J. Atm. and Oceanic Tech.*, **3**, pp. 422–432, 1986.
41. A.V. Oppenheim and A.S. Willsky, *Signals and Systems*, Prentice Hall, Englewood Cliffs, NJ, 1983.
42. P. Pampaloni and S. Paloscia, Microwave Emission and Plant Water Content: A Comparison Between Field Measurement and Theory, *IEEE Trans. Geosci. Remote Sensing*, **24**, pp. 900–904, 1986.
43. G.A. Poe, Optimum Interpolation of Imaging Microwave Radiometer Data, *IEEE Trans. Geosci. Rem. Sens.*, **GE-28**, pp. 800–810, 1990.
44. Q.P. Remund, D.E. Early, and D.G. Long, Optimization of SIRF for NSCAT, Microwave Earth Remote Sensing Laboratory internal report, Brigham Young University, Provo, UT, MERS#96-003, 3 July, 1999. (Available via <http://www.mers.byu.edu/Papers/reports>).
45. F. Remy, M. Ledroit, and J.F. Minster, Katabatic Wind Intensity and Direction over Antarctica Derived from Scatterometer Data, *Geophys. Res. Letters*, **19**, pp. 1021–1024, 1992.
46. W.D. Robinson, C. Kummerow, and W.S. Olson, A Technique for Enhancing and Matching the Resolution of Microwave Measurements from the SSM/I Instrument, *IEEE Trans. Geosci. Rem. Sens.*, **30**, 3, pp. 419–429, 1992.
47. R. Sethmann, B.A. Burns, and G.C. Heygster, Spatial Resolution Improvement of SSM/I Data with Image Restoration Techniques, *IEEE Trans. Geosci. Rem. Sens.*, **32**, 6, pp. 1144–1151, 1994.
48. B. Sharpe and A. Kerr, Multichannel Fusion Techniques for Resolution Enhancement During Ground Processing, *Proc. Int. Geosci. Rem. Sens. Sym.*, Espoo, Finland, pp. 1495–1462, 1991.
49. K.V. Shettigara, A Linear Transformation Technique for Spatial Enhancement of Multispectral Images Using a Higher Resolution Data Set, *Proc. Int. Geosci. Rem. Sens. Sym.*, pp. 2615–2618, 1989.
50. M.W. Spencer, C. Wu, and D.G. Long, Improved Resolution Backscatter Measurements with the SeaWinds Pencil-Beam Scatterometer, *IEEE Trans. Geosci. Remote Sens.*, **38**, 1, pp. 89–104, 2000.
51. H. Stephen and D.G. Long, Multi-spectral Analysis of the Amazon Basin using Sea-

- Winds, ERS, Seasat Scatterometers, TRMM-PR and SSM/I, *Proc. Int. Geosci. Rem. Sens. Sym.*, Toronto, Canada, 24–28 June, pp. 1780–1782, 2002.
52. P. J. Stephen and A.S. Jones, Computationally Efficient Discrete Backus–Gilbert Footprint-Matching Algorithm, *IEEE Trans. Geosci. Rem. Sens.*, **40**, 8, pp. 1865–1878, 2002.
53. A. Stogryn, Estimates of Brightness Temperatures from Scanning Radiometer Data, *IEEE Trans. Antennas Propagat.*, **AP-26**, 5, pp 720–726, 1978.
54. R.H. Thomas, R.A. Bindshadler, R.L. Cameron, F.D. Carsey, B. Holt, T.J. Hughes, C.W.M. Swithinbank, I.M. Whillans, and H.J. Zwally, Satellite Remote Sensing for Ice Sheet Research, *NASA Technical Memorandum*, 86233, 27, 1985.
55. F.T. Ulaby, R.K. Moore, and A.K. Fung, *Microwave Remote Sensing — Active and Passive*, Vols. 1 and 2, Addison–Wesley Publishing Co., Reading, Mass., 1981.
56. N.P. Walker, Limitations of the possible resolution enhancement of ERS-1 scatterometer images, *IEEE Trans. Geosci. Rem. Sens.*, **35**, 1, pp. 196–198, 1997.
57. F.J. Wentz, Measurement of Oceanic Wind Vector Using Satellite Microwave Radiometers, *IEEE Trans. Geosci. Rem. Sens.*, **30**, 5, pp. 960–972, 1992.
58. M.E. Willis, *Algebraic Reconstruction Algorithms for Remote Sensing Image Enhancement*, Master’s Thesis, Brigham Young University, Provo, Utah, 2000.
59. V.R. Wismann, K. Boehnke, and C. Schmullius, Monitoring Ecological Dynamics in Africa with the ERS-1 Scatterometer, *Proc. Int. Geosci. Rem. Sens. Sym.*, pp. 1523–1525, 1995.